Hysteretic Tuned Mass Dampers for Seismic Protection

A.Boccamazzo, B. Carboni, G. Quaranta, W. Lacarbonara
Department of Structural and Geotechnical Engineering,
Sapienza University of Rome, Rome 00184, Italy,
antonio.boccamazzo@uniroma1.it, biagio.carboni@uniroma1.it,
giuseppe.quaranta@uniroma1.it, walter.lacarbonara@uniroma1.it

February 7, 2021

Abstract. The main shortcoming of linear Tuned Mass Dampers employed as anti-seismic device, is related to the loss of tuning, also called *detuning*, due to changes in the structural stiffness that may occur after the onset of damage. To take into account this detrimental effect, in this study the main system is represented through a hysteretic nonlinear constitutive model. An identification procedure to fast identify the dynamic behavior of a multistory steel-scale structure is presented. Moreover, in the present work an absorber that exhibits a hysteretic restoring force with pinching is considered. The goal is to tune the nonlinear behavior of the TMD with the nonlinear behavior of the structure to control to make the TMD effective for seismic applications overcoming the detuning effect.

Keywords: Hysteretic TMD, Nonlinear identification, TMD optimization

1. Introduction

Tuned Mass Dampers (TMDs) are recognized as effective device to mitigate wind-induced vibrations in civil structures whereas their seismic protection capability still represents an open issue (Elias and Matsagar, 2017). The main shortcoming is related to the loss of tuning, or *detuning*, due to changes in the structural stiffness that may occur after the onset of damage (Wong and Harris, 2012). To take into account this detrimental effect, the main system is represented through a hysteretic constitutive model (Boccamazzo et al., 2018).

Moreover, since real structures exhibit nonlinear behavior even at relatively low amplitudes and linear TMDs can suffer the drawback of detuning, in the present work an absorber that exhibits a hysteretic restoring force with pinching is considered (Carboni et al., 2015; Carboni and Lacarbonara, 2016). In order to make the TMD effective for seismic applications, the objective of the present study is to tune the nonlinear behavior of the TMD with the nonlinear behavior of the structure.

With the goal of considering realistic structures, the main system parameters are evaluated considering the experimental data previously collected for a five-story scale building model (Carboni and Lacarbonara, 2016). Since the structure shows a nonlinear dynamic behavior (specifically, softening backbone), it is well described by the Bouc-Wen model. After an extensive discussion about the dynamic properties of this hysteretic model, a new analytic identification procedure to fast identify the dynamic behavior of the structure is presented. This identification is compared with

the results obtained by a second numerical identification that exploits the Differential Evolutionary strategy (Boccamazzo et al., 2020).

Later, a new optimization procedure for the TMD constitutive parameters search, proposed in (Boccamazzo et al., 2020), is implemented. Finally, the vibration mitigation performances of the optimized hysteretic TMDs mounted on the nonlinear main system are carefully evaluated.

2. The Bouc-Wen model of hysteresis

The Bouc–Wen (BW) is one of the most popular model used to describe non-linear hysteretic systems. It was introduced by Bouc (Bouc, 1967) and later extended by Wen (Wen, 1976) who showed its versatility in producing a variety of hysteretic patterns.

The overall restoring force of the BW model is:

$$f(x) = k_e\, x + z(x). \tag{1}$$

It is the sum of a linear elastic force (denoted by $k_e x$, where x is the displacement and k_e the elastic stiffness) and a hysteretic force (denoted by z) whose evolution in time is given by the following first-order differential equation:

$$\dot{z} = \{k_d - [\gamma + \beta\,\mathrm{sgn}(\dot{x}z)]|z|^n\}\dot{x}, \tag{2}$$

where the overdot denotes differentiation with respect to time, the parameters γ and β are related to the hysteresis shape, n rules the transition between the elastic and post-elastic phase. The stiffness k_d is a fraction of the initial stiffness at the origin $k_0 = k_e + k_d$. The tangent stiffness (denoted by z_x) of the hysteretic force is:

$$\frac{dz}{dx} = z_x = [k_d - (\gamma + \beta\,\mathrm{sgn}(\dot{x}z)]|z|^n. \tag{3}$$

It is possible to devise three different nonlinear behaviors during loading ($\dot{x} > 0$): softening hysteresis (stiffness degrading) if $\gamma + \beta > 0$, quasilinear hysteresis (constant stiffness) if $\gamma + \beta = 0$, and hardening hysteresis (stiffness increasing) if $\gamma + \beta < 0$. A collection of these types of hysteresis loops are shown in Fig. 1.

Depending on the signs of z ad $\dot{x}$, the hysteretic cycles can be divided into four branches; the different branches are shown in Fig. 2, where the characteristic displacements, namely the transition points that divide the four branches, are also indicated. In particular $x_0 = -x_2$ are the maximum displacements reached, and $x_1 = -x_3$ are the points where the hysteretic force vanishes. Each of them admits the general solution reported in Tab. I. The terms b_1, b_2, b_3, b_4 are constants of integration that can be found imposing the initial conditions.

The hysteretic force reaches the maximum when the z_x tends to zero. Consequently, imposing the stationarity of z, the upper and the lower bounds are given by

$$z_{max} = -z_{min} = \frac{k_d}{\gamma + \beta}. \tag{4}$$

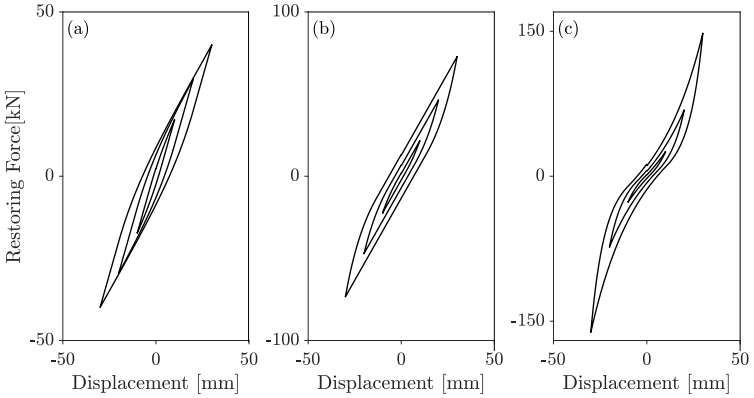

Figure 1. Loops of the total restoring force for (a) softening hysteresis ($\gamma = \beta = 0.05$ mm^{-1}), (b) quasilinear hysteresis ($-\gamma = \beta = 0.05$ mm^{-1}), (c) hardening hysteresis ($\gamma = -0.08$ mm^{-1} and $\beta = 0.05$ mm^{-1}), described by the BW model when $k_e = k_d = 1$ kN/mm and $n = 1$.

Table I. BW model solution for each branch.

Branch	z	$\dot{x}$	z_x	z
1	> 0	< 0	$k_d + (\gamma - \beta)z$	$\frac{k_d}{\gamma-\beta} + b_1 e^{x(\beta-\gamma)}$
2	< 0	< 0	$k_d - (\gamma + \beta)z$	$-\frac{k_d}{\gamma+\beta} + b_2 e^{x(\beta+\gamma)}$
3	> 0	< 0	$k_d - (\gamma - \beta)z$	$\frac{k_d}{-\gamma+\beta} + b_3 e^{x(-\beta+\gamma)}$
4	> 0	> 0	$k_d + (\gamma + \beta)z$	$\frac{k_d}{\gamma+\beta} + b_4 e^{x(-\beta-\gamma)}$

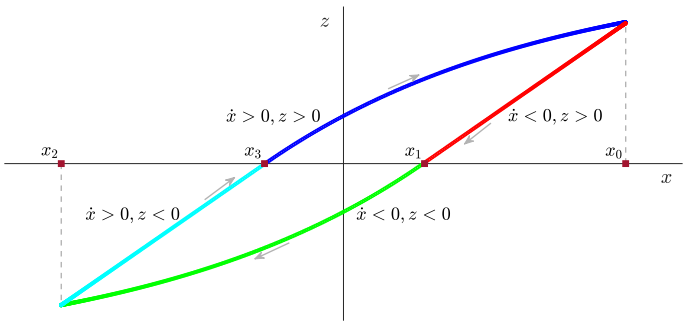

Figure 2. Typical force-displacement hysteretic cycles. The four branches are highlighted by the red, green, cyan and blue line and the transition points are described by the characteristic displacement x_0, x_1, x_2,and x_3,

Consider the closed form solution of the loading branch of the BW model (branch 4 in Tab. I). Imposing the initial condition $z(0) = 0$ is possible to find the constant $b_4 = -\frac{k_d}{\gamma+\beta}$ and, hence, the

particular solution of the first loading (z_{fl}) branch reads

$$z_{fl}(x) = \frac{(1 - e^{-x(\gamma+\beta)})k_d}{\gamma + \beta}. \tag{5}$$

This solution is a monotonically increasing exponential function and the value of z_{max} represents an horizontal asymptote such that $\lim_{x\to\infty} z_{fl}(x) = z_{max}$. For this reason it makes sense to define a saturation displacement for which the hysteretic force is close to the asymptotic value. This characteristic displacement, defined as x_{95}, is found imposing that the $z(x_{95}) = 0.95\, z_{max}$. Its meaning is shown in the Fig. 3. After few simple steps it can be stated that

$$x_{95} = \frac{-ln(0.05)}{\gamma + \beta} \simeq \frac{3}{\gamma + \beta}. \tag{6}$$

Therefore, the stiffness corresponding to this point is:

$$k_{d95} = \frac{0.95\, z_{max}}{x_{95}} = \frac{0.95\, k_d}{-ln(0.05)} \simeq 0.317\, k_d. \tag{7}$$

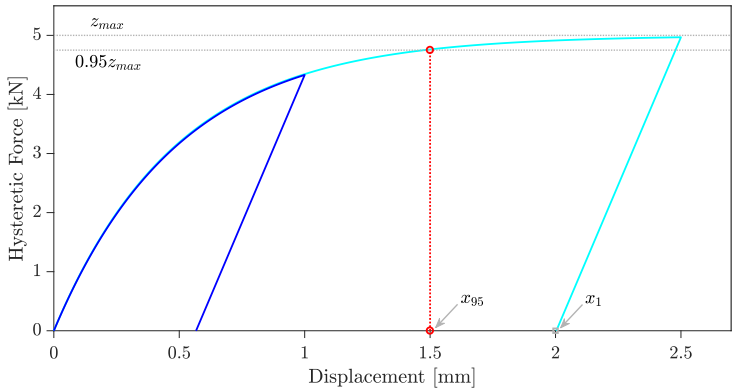

Figure 3. The meaning of x_{95} for the BW model, when $k_d = 10$ kN/mm, $\gamma = \beta = 1$ mm^{-1} and $n = 1$.

Consider a single-degree-of-freedom (SDOF) system composed by a mass m connected to the ground through a nonlinear spring that exerts the restoring hysteretic force $f(x)$ (function of the displacement x) described by the BW model. The equation of motion of the SDOF system reads:

$$m\ddot{x} + f(x) = -m\ddot{x}_g, \tag{8}$$

$$f(x) = k_e x + z(x), \tag{9}$$

$$\dot{z} = \{k_d - [\gamma + \beta\, \mathrm{sgn}(\dot{x}z)]|z|^n\}\dot{x}, \tag{10}$$

where $\ddot{x}_g$ is the base acceleration. In Fig. 4 the Frequency Response Curves (FRCs) for a hysteretic oscillator with $m = 1$ kg, $k_e = 10$ N/m, $k_d = 30$ N/m, $\gamma = \beta = 0.5$ mm^{-1} , and $n = 1$ are shown.

Note that the system is characterized by an initial (f_{in}) and an ultimate (f_{ult}) resonance frequencies for small and large oscillation amplitude, respectively, determined as follows

$$f_{ul} = \frac{1}{2\pi}\sqrt{\frac{k_e}{m}} = 1.00\,\text{Hz} \tag{11}$$

$$f_{in} = \frac{1}{2\pi}\sqrt{\frac{k_e+k_d}{m}} = 0.50\,\text{Hz} \tag{12}$$

The relationship between natural frequency and amplitude is commonly known as Backbone Curve and it is represented by the red dashed line in Fig. 4. It should be noted that the backbone passes through the point highlighted in blue (x_{95}, f_{95}), where

$$f_{95} = \frac{1}{2\pi}\sqrt{\frac{k_e+0.317k_d}{m}} = 0.70\,\text{Hz} \tag{13}$$

$$x_{95} = \frac{3}{\gamma+\beta} = 3.00\,\text{mm} \tag{14}$$

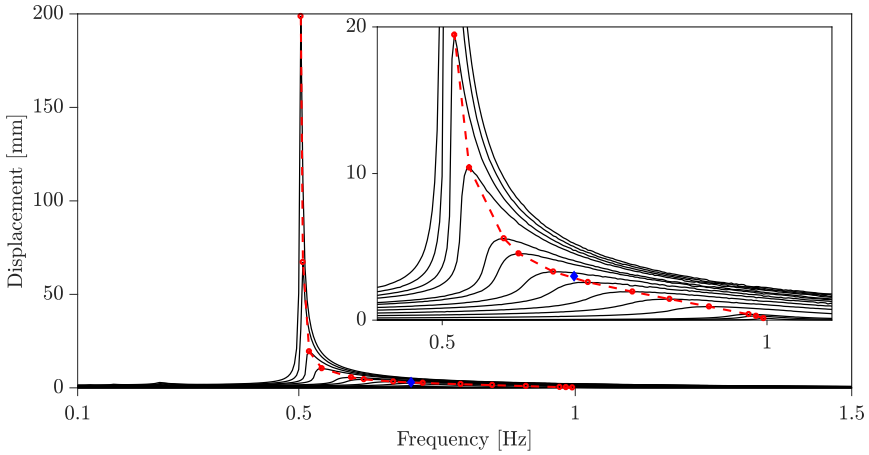

Figure 4. FRCs (in black), Backbone Curves (in red) and the point (f_{95}, x_{95}) (in blue) for the Hysteretic Oscillator, charcterized by the constitutive parameters: $m = 1$ kg, $k_e = 10$, N/m, $k_d = 30$ N/m, $\gamma = \beta = 0.5$ mm^{-1} , and $n = 1$.

The damping ratio is computed by exploiting the equivalence with the dissipated energy of the linear viscoelastic oscillator whose restoring force is $f_l(x) = c\dot{x} + k_e x$ where c is the linear damping coefficient. The damping ratio is defined as

$$\xi_0 = \frac{c}{c_{cr}}. \tag{15}$$

Substituting in Eq. (15) the critical damping coefficient $c_{cr} = 2\omega_0 m$, where $\omega_0 = \sqrt{k/m}$ is natural pulsation (in radians), it holds

$$\xi_0 = \frac{c\,\omega_0}{2\,k_e} \tag{16}$$

The elastic energy is

$$\mathcal{E}_E = \frac{1}{2}\,k_e\,x_0^2 \tag{17}$$

while the dissipated energy reads

$$\mathcal{E}_D = \pi\, c\, \overline{\omega}\, x_0^2 \tag{18}$$

where $\overline{\omega}$ is excitation pulsation. Making explicit the terms k and c from Eqs. (17) and (18), respectively, the damping ratio can be written as:

$$\xi_0 = \frac{\mathcal{E}_D}{4\,\pi\,\mathcal{E}_E}\frac{\omega_0}{\overline{\omega}} \tag{19}$$

The pulsation ratio, namely the ratio between the natural pulsation of the system and that of the external excitation, is usually set to 1, so that the damping ratio is computed as

$$\xi_0 = \frac{\mathcal{E}_D}{4\,\pi\,\mathcal{E}_E}. \tag{20}$$

The damping ratio and the dissipated end elastic energies are shown in Figs. 5-(a) and 5-(b), respectively.

The dissipated energy of the Hysteretic Oscillator is calculated as the area enclosed by the force-displacement curve during a sinusoidal displacement cycle (with maximum displacement x_0), so that

$$\mathcal{E}_D = \int_{-x_0}^{x_0} z\, dx. \tag{21}$$

For very large displacement, as shown in Fig. 5-(a), this dissipated area can be approximated as

$$\mathcal{E}_D \simeq 4\, z_{max}\, x_0. \tag{22}$$

Substituting Eqs. (4) and (22), the damping ratio ξ_0 can be expressed as funtion of the displacement x

$$\overline{\xi}_0(x) = \frac{2\,k_d}{k_e \pi(\gamma+\beta)\,x}. \tag{23}$$

In a novel variant of the BW model proposed in (Carboni et al., 2015) a function $H(x)$ is introduced in order to provide a pinching along the force-displacement cycle. This is described by the following exponential function:

$$H(x) = 1 - \xi_H e^{-x^2/x_H} \tag{24}$$

where $\xi_H \in [0,1)$ and $x_H > 0$. Specifically, the function $H(x)$ modulates the tangent stiffness k_d of the BW model in the neighborhood of the origin. Therefore, the evolution in time of the hysteretic force is described as follows:

$$\dot{z} = \{k_d H(x) - [\gamma + \beta\,\mathrm{sgn}(\dot{x}z)]|z|^n\}\dot{x}. \tag{25}$$

The pinching function $h(x)$ depends on two parameters, namely, ξ_h and x_H. The first one governs the intensity of the pinching effect, while the latter regulates the width of the pinched region of the hysteresis loop. Specifically, low values of x_H entail a localized pinching around the origin of the force-displacement cycles, whereas high values determine the pinching presence over a larger

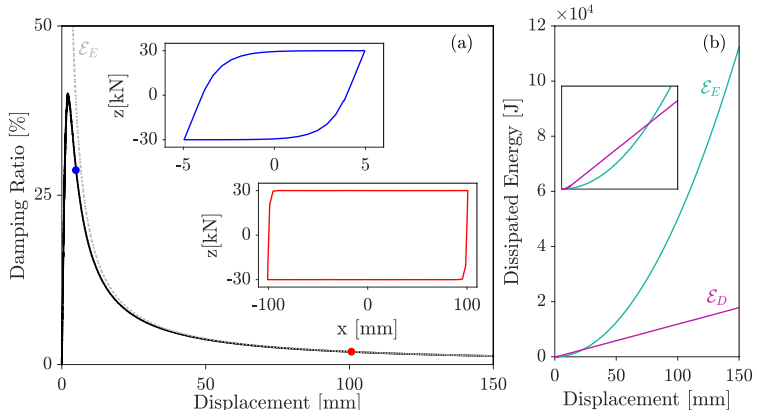

Figure 5. Damping ratio (black solid line), Eq. (23) (dashed grey line), and force-displacement cycles (blue and red solid lines) in (a). Elastic and Dissipated Energies in (b).

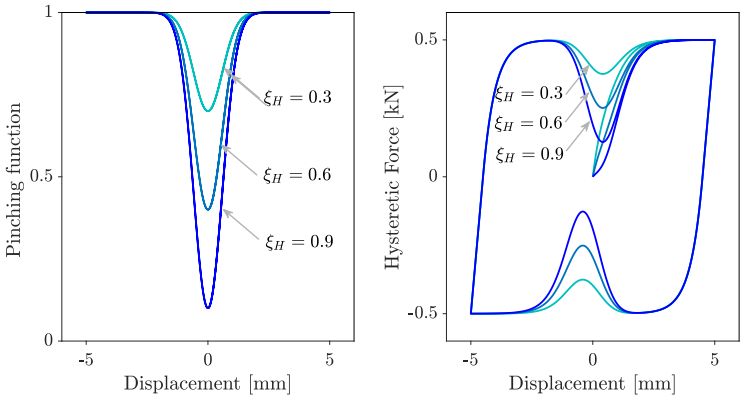

Figure 6. Effect of the parameter ξ_H on the pinching function $H(x)$ (left) and on the hysteretic force $z(x)$ (right). In all plots $k_d = 1$ kN/mm, $\gamma = \beta = 1$ mm^{-1}, $x_H = 0.7$ mm^2, $n = 1$ while ξ_H is set to 0.3, 0.6 and 0.9.

displacement range. Obviously, the modified BW model can be consider a generalization of the BW model, since the modified model returns the classical model when ξ_H is null. The effects of the parameter ξ_H and x_H on the hysteretic force $z(x)$ and pinching function $H(x)$ are shown in Figs. 6 and 7.

3. Mechanical model and equations of motion

The main structure and the TMD are modeled as a SDOF system: specifically, the first one by employing the BW model, while the latter, by means of the pinched variant previously described. Indeed, the the overall elastoplastic behavior of the steel structure is well described by means of the classical BW model of hysteresis. The pinched BW model is able to simulate a large variety of nonlinear behaviors within the context of novel absorbers, instead. Particularly, it intends to

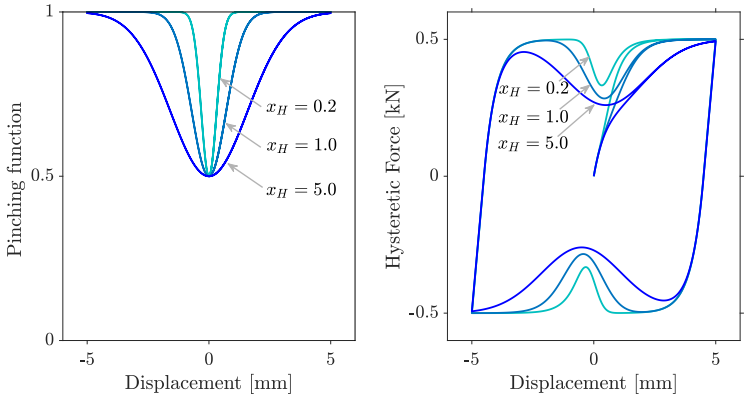

Figure 7. Effect of the parameter x_H on the pinching function $H(x)$ (left) and on the hysteretic force $z(x)$ (right). In all plots $k_d = 1$ kN/mm, $\gamma = \beta = 1$ mm^{-1}, $\xi_H = 0.5$, $n = 1$ while x_H is set to 0.2, 1 and 5 mm^2.

simulate here a nonlinear TMD, consisting of a single mass that dissipates hysteretic energy through suitable assemblies of NiTiNOL and steel wire ropes, that has been characterized experimentally and numerically in the context of previous studies (Carboni et al., 2015; Carboni and Lacarbonara, 2016), in which were demonstrated that the pinching behavior is due to the coupling of frictional dissipation and phase transformations in SMA material. As a consequence, the protected structure turns out to be a nonlinear two-degree-of-freedom system (2DOF).

Its schematic is given in Fig. 8. The structure displacement is indicated as x_1; x_2 is the dispacement relative to the main structure, x_g is the ground displacement: so that, $p_1 = x_g + x_1$ and $p_2 = x_g + x_1 + x_2$ are the absolute dispacement of structure and TMD, respectively. The terms $f_1(x_1) = k_{e1}x_1 + z_1(x_1)$ and $f_2(x_2) = k_{e2}x_2 + z_2(x_2) + k_{c2}x_2^3$ are the overall nonlinear restoring forces of structure and TMD, respectively. Note that the cubic elastic term $k_{c2}x_2^3$ is also introduced to take into account the effect of a hardening behavior in the absorber restoring force.

The equations of the motion of the 2DOF system under seismic base acceleration are given hereafter, where the time dependence will be tacitly omitted for the ease of notation.

$$m_1\ddot{x}_1 + k_{e_1}x_1 + c_1\dot{x}_1 + z_1 - k_{e_2}x_2 - k_{c2}x_2^3 - z_2 = -m_1\ddot{x}_g, \tag{26}$$

$$m_2\ddot{x}_2 + m_2\ddot{x}_1 + k_{e_2}x_2 + k_{c2}x_2^3 + z_2 = -m_2\ddot{x}_g, \tag{27}$$

$$\dot{z}_1 = \{k_{d1} - [\gamma_1 + \beta_1 \operatorname{sgn}(\dot{x}_1 z_1)]|z_1|^{n_1}\}\dot{x}_1, \tag{28}$$

$$\dot{z}_2 = \{k_{d2}H(x_2) - [\gamma_2 + \beta_2 \operatorname{sgn}(\dot{x}_2 z_2)]|z_2|^{n_2}\}\dot{x}_2. \tag{29}$$

Hereafter, the subscript 1 indicates the quantities that refer to the main structure, while the subscript 2 indicates the quantities that refer to the absorber.

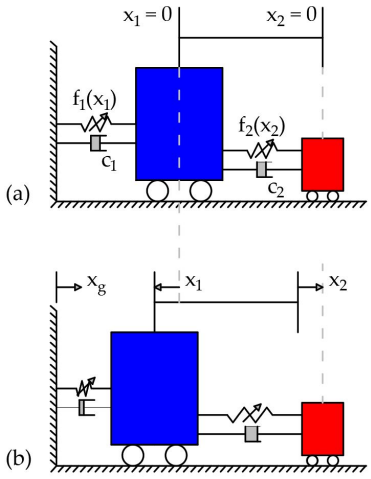

Figure 8. Schematic of two-DOF model; undeformed (a) and deformed (b) configuration.

4. Analytical and numerical nonlinear structural identifications

The steel multistory structure analysed in (Carboni and Lacarbonara, 2016) is here considered. The experimental data (the blue line in Fig. 9) show a softening behavior characterized by a decrease of the main resonance frequency and simulated through the BW oscillator.

The parameters to be identified are collected in the vector $\boldsymbol{\theta} = \{k_{e_1}, k_{d_1}, \gamma_1, \beta_1\}$ while n_1 is set to 1. The weight of the main structural mass is estimated to be 565.82 kg. Two strategies of identification are proposed.

The first strategy is analytic and exploits the relationship previously introduced. The parameters $\overline{k}_{e1}$, $\overline{k}_{d1}$, $\overline{\gamma}_1$ and $\overline{\beta}_1$ are determined as follows.

$$\overline{f}_{ul} = \frac{1}{2}\sqrt{\frac{\overline{k}_{e1}}{m_1}} = 4.23\,\text{Hz} \rightarrow \overline{k}_{e1} = 0.3610\,\text{kN/mm} \tag{30}$$

$$\overline{f}_{in} = \frac{1}{2}\sqrt{\frac{\overline{k}_{e1}+\overline{k}_{d1}}{m_1}} = 4.02\,\text{Hz} \rightarrow \overline{k}_{d1} = 0.0387\,\text{kN/mm} \tag{31}$$

$$\overline{f}_{95} = \frac{1}{2}\sqrt{\frac{\overline{k}_{e1}+0.317\,\overline{k}_{ed}}{m_1}} = 4.0875\,\text{Hz} \rightarrow \overline{x}_{95} \cong 10\,\text{mm} \tag{32}$$

$$\overline{x}_{95} = \frac{3}{\overline{\gamma}_1+\overline{\beta}_1} \rightarrow \overline{\gamma}_1 + \overline{\beta}_1 = 0.30\,\text{mm}^{-1} \tag{33}$$

and setting $\overline{\gamma}_1$ equal to $\overline{\beta}_1$ it results $\overline{\gamma}_1 = 0.15$ mm $^{-1}$.

The second strategy is numerical and exploits the Differential Evolution (DE) algorithm (Storn and Price, 1997). The DE algorithm is implemented to find the minimum of the following objective function:

$$\Phi_{id}(\boldsymbol{\theta}) = \sum_{i=1}^{M} w_f \frac{(f_{ex,i} - f_{m,i}(\boldsymbol{\theta}))}{f_{ex,i}} + w_\xi \frac{(\xi_{ex,i} - \xi_{m,i}(\boldsymbol{\theta}))}{\xi_{ex,i}}. \tag{34}$$

For the ith base excitation amplitude, this objective function measures the difference between the experimental frequencies and damping ratios ($f_{ex,i}$ and $\xi_{ex,i}$, respectively) and those numerically estimated ($f_{m,i}$ and $\xi_{m,i}$, respectively). The weight functions w_f and w_ξ can promote the agreement in frequency or damping identification. The BW damping is estimated by means of Eq. (20).

In order to save time, a new identification procedure is, here, proposed. Indeed, the standard identification strategy needs the evaluation of the entire FRC, for different oscillation amplitude, to get its peak so as to build the backbone. Obviously, the FRC evaluation requires the stationary response of the SDOF in several points. In the proposed method a harmonic displacement is imposed and the overall restoring force is evaluated. In this way is possible to build the force-displacement cycles. The resonance frequency is estimated from the average stiffness along the hysteresis cycles as follows:

$$k(x) = \frac{\int_{\mathcal{C}} k_e + z_x(x)dx}{\int_{\mathcal{C}} dx}, \tag{35}$$

where $\mathcal{C}$ is the displacement path along the loading and unloading branches. The proposed method is very fast because it requires only one stationary response of the SDOF for each excitation level. It is worth noting another great advantage of proposed method: since the displacement is imposed, the oscillation amplitude at the resonance frequency is known.

The identified structural parameters, according to the two different approaches, are listed in table II. Several identifications are carried out by considering different weight functions.

Table II. Identified structural parameters by exploiting the analytical and numerical approaches for different weight functions.

	w_f [–]	w_d [–]	k_{e1} $\left[\frac{\text{kN}}{\text{mm}}\right]$	k_{d1} $\left[\frac{\text{kN}}{\text{mm}}\right]$	γ_1 $\left[\frac{\text{kN}^{1-n}}{\text{mm}}\right]$	β_1 $\left[\frac{\text{kN}^{1-n}}{\text{mm}}\right]$	n_1 [–]
Analytical	–	–	0.3610	0.0387	0.150	0.150	1
DE	0.7	0.3	0.356	0.058	0.312	0.076	1
DE	0.5	0.5	0.352	0.057	0.262	0.057	1
DE	0.1	0.9	0.354	0.032	0.001	0.126	1

Fig. 9 and Fig. 10 show the frequency and damping identified, respectively. In order to promote the agreement in frequency rather than that in damping, and since the experimental damping ratio is low and it does not affect much the structural behavior, from now on, let us to consider the weight coefficients w_e and w_d equal to 0.7 and 0.3, respectively.

5. TMD optimization and seismic performances

The TMD optimization strategy is formulated in the time domain and it is suitable for generally nonstationary base excitations. The DE algorithm is employed to look for the maximum of the objective function:

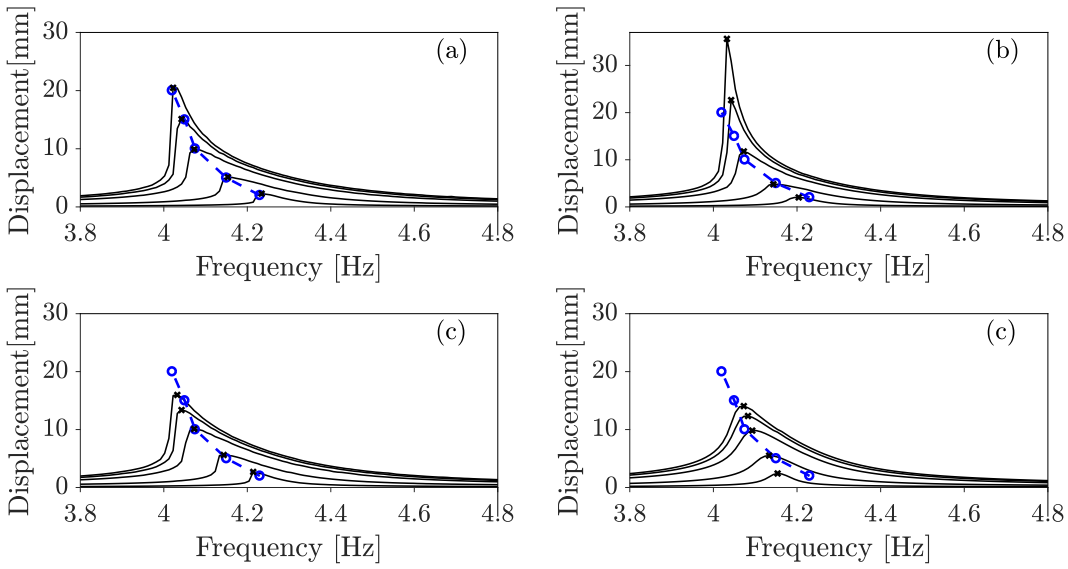

Figure 9. Displacement Frequency Response Function of the identified BW model (black line) and experimental data (blue line). Case a) $w_f = 0.7$, $w_d = 0.3$, b) analytic, c) $w_f = 0.5$, $w_d = 0.5$, d) $w_f = 0.1$, $w_d = 0.9$.

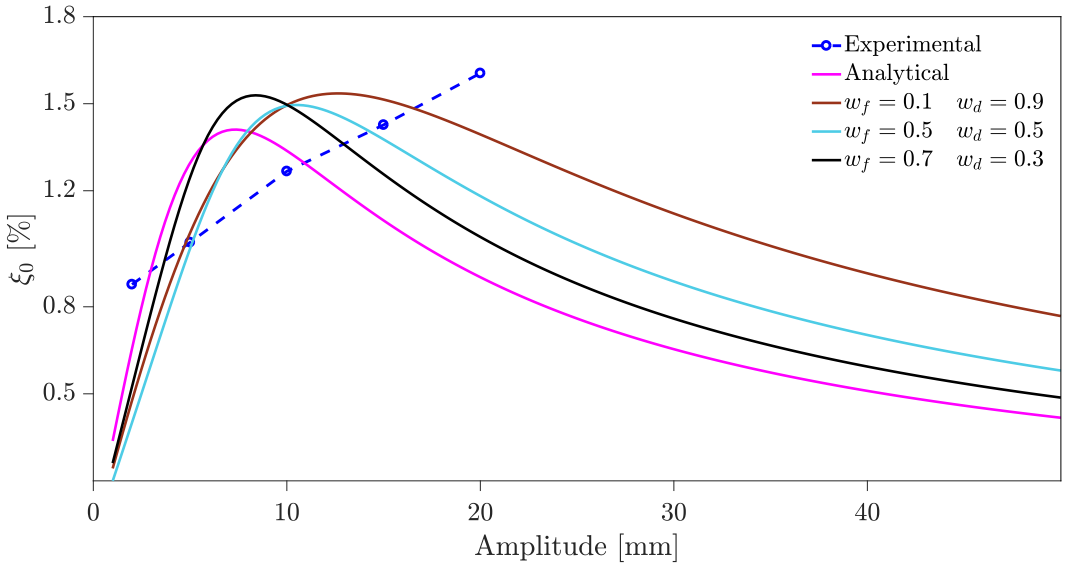

Figure 10. Damping of the identified BW model (solid line) for different weight functions and experimental data (dashed-blue line).

$$R_t(\mathbf{d}) = 1 - \frac{\sum_{r=1}^{S} \text{rms}[x_r^{con}(\mathbf{d})]}{\sum_{r=1}^{S} \text{rms}[x_r^{unc}]}. \tag{36}$$

Herein, $x_r^{con}(\mathbf{d})$ and x_r^{unc} denote the displacement of the controlled and uncontrolled system (Fig. 11) under the rth seismic acceleration time history, with $r = 1, \ldots, S$. This function represents the ratio between the sum of the controlled and uncontrolled root mean squares (rms) of the main system displacement under a set of earthquakes.

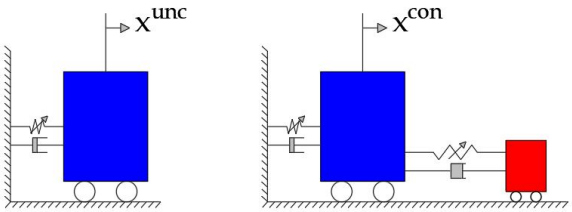

Figure 11. Uncontrolled (left) and controlled (right) scenarios.

The TMD parameters are collected in the vector $\mathbf{d}$ and their optimal are found by exploiting again the DE strategy. The design space of the TMD parameters is given in Tab. III, where the bounds are expressed as function of the structural parameters. The parameter n_2 is set equal to 1, while the upper limit for ξ_H is posed to 0.985 to avoid numerical problem.

Table III. Design space of the TMD model parameters.

	k_{e_2} $\left[\frac{\text{kN}}{\text{mm}}\right]$	k_{d_2} $\left[\frac{\text{kN}}{\text{mm}}\right]$	k_{c2} $\left[\frac{\text{kN}}{\text{mm}^3}\right]$	γ_2 $\left[\frac{\text{kN}^{1-n_1}}{\text{mm}}\right]$	β_2 $\left[\frac{\text{kN}^{1-n_1}}{\text{mm}}\right]$	ξ_H [–]	x_H $[\text{mm}^2]$
Lower bound	$\frac{k_{e_1}}{1000}$	$\frac{k_{e_1}}{1000}$	0	$\frac{\gamma_1}{1000}$	$\frac{\beta_1}{1000}$	0	20
Upper bound	$10k_{e_1}$	$30k_{e_1}$	k_{e1}	$100\gamma_1$	$100\beta_1$	0.985	40000

A set of 8 spectrum-compatible seismic acceleration time histories are generated: one half of this set is defined so that their spectra match the design spectrum for the Immediate Occupancy Limit State (SLD), while the second half the Life Safety Limit State (SLV). The design spectra are defined in in agreement with the Italian Building Code (NTC, 2018) (SLV and SLD have a probability of occurrence equal to 10% and 63% in 50 years, respectively) and the reference site is the city of Messina (Italy). The characteristic parameters for the elastic response spectra (namely the design ground acceleration, the spectral amplification factor, and the upper limit of the period of the spectral plateau) are the following: $a_g = 0.082\,g$, $F_0 = 2.318$, $T_c^* = 0.294$ s for SLD, and $a_g = 0.247\,g$, $F_0 = 2.411$, $T_c^* = 0.359$ s for SLV. Three different values for the mass ratio $\mu = m_2/m_1$ are considered, i.e. $\mu = (0.01, 0.02, 0.05)$. The convergence of the objective function

R_t, defined in Eq. (36), is shown in Fig. 12 for different mass ratios. Hysteretic TMDs endowed with mass ratios equal to 0.01, 0.02, and 0.05 attain meaningful reductions of the RMS of the main system displacement, namely, 40%, 50%, 60%, respectively.

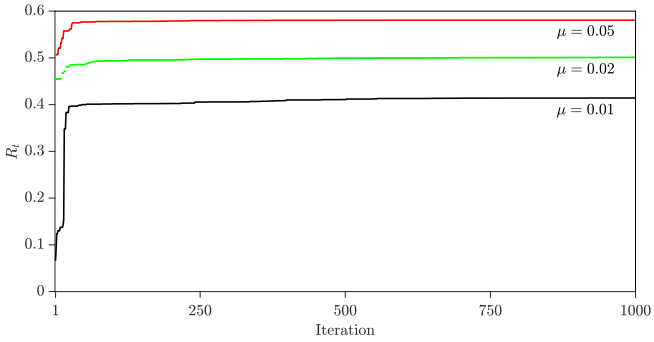

Figure 12. Convergence of the objective function R_t shown in Fig. 4. RMS displacement reductions for the controlled structure. The mass ratios are set to 0.01 (black line), 0.02 (green line), and 0.05 (red line).

After just 50 iterations, the optimizer sets to zero the k_{c2} for all the population vectors as shown in Fig. 13. If all the vector converge to a unique value, that value get fixed and it can not longer be turned in the following iterations. Obviously, this means that the optimized solution does not need the addition of the cubic elastic stiffness. Therefore, these results confirm the above conclusion: since the structure has a softening behavior, the optimized TMD has to exhibit a similar behavior characterized by softening. In this way the TMD can be tuned (remaining effective) with the system for a larger range of oscillation amplitude. The optimal TMD parameters are reported in Tab. IV.

Table IV. Optimum parameters of the TMD for the steel structure (set TMD-NS) from time domain-based optimization under nonstationary excitation.

μ	Unit	0.01	0.02	0.05
k_{e_2}	[kN/mm]	$3.31 \cdot 10^{-3}$	$6.41 \cdot 10^{-3}$	$1.41 \cdot 10^{-2}$
k_{d_2}	[kN/mm]	$9.19 \cdot 10^{-2}$	$2.35 \cdot 10^{-2}$	$6.19 \cdot 10^{-2}$
γ_2	[kN$^{1-n_2}$/mm]	$9.92 \cdot 10^{-2}$	$1.00 \cdot 10^{-3}$	$3.91 \cdot 10^{-4}$
β_2	[kN$^{1-n_2}$/mm]	$6.77 \cdot 10^{-2}$	$1.65 \cdot 10^{-1}$	$4.49 \cdot 10^{-1}$
ξ_H	[–]	0.985	0.898	0.870
x_H	[mm^2]	$4.00 \cdot 10^4$	$2.54 \cdot 10^3$	$2.00 \cdot 10^2$

Finally, the seismic effectiveness of the hysteretic TMD in protecting the identified structure is discussed by considering 3 new sets of 7 seismic acceleration time histories. The assortments are compatible with the SLD, SLV and SLC (Collapse Prevention Limit State, $a_g = 0.336\,g$, $F_0 = 2.446$,

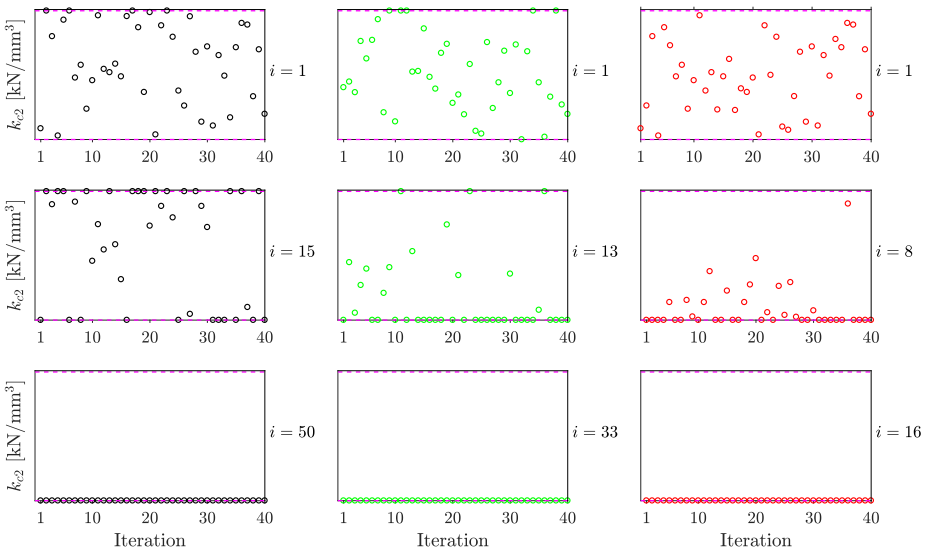

Figure 13. Cubic elastic stiffness k_{c2} for the population vectors at ith iteration. The dashed lines represent the lower and upper bounds of the search space. The mass ratios are set to 0.01 (black line), 0.02 (green line), and 0.05 (red line).

$T_c^* = 0.384$ s), respectively. The results are reported in Tab. V and clearly show that a nonlinear TMD reduces the loss of mitigation capability caused by the detuning effect.

Table V. Objective function R_t for each limit state.

μ	SLD	SLV	SLC
0.01	0.42	0.38	0.35
0.02	0.49	0.45	0.41
0.05	0.58	0.51	0.46

6. Conclusions

The present work is focused on the identification of a steel structure exhibiting a nonlinear dynamic behavior (specifically, softening backbone) and on the design of a passive hysteretic TMD for seismic protection purposes. Two identification strategies are proposed: the first strategy is analytic and exploits the properties of the BW model, while the latter is numerical and is based on the use of

DE. Numerical results have proven that the optimized hysteretic TMD has the ability to reduce the main structure vibrations under strong seismic base accelerations by exploiting its softening behavior similar to that exhibited by the main structure. Indeed, reduction of the RMS displacement close to 40% (for the SLV) were obtained with the hysteretic TMD endowed with a mass ratio equal to 1%. It has also been shown that adopting a TMD endowed with a nonlinear cubic stiffness does not improve mitigation performances.

References

Boccamazzo, A., B. Carboni, G. Quaranta, and W. Lacarbonara. Optimized Hysteretic TMD for Seismic Control of a Nonlinear Steel Structure. In *ASME 2018 International Design Engineering Technical Conferences and Computers and Information in Engineering Conference*. American Society of Mechanical Engineers Digital Collection, 2018.

Boccamazzo, A., B. Carboni, G. Quaranta, and W. Lacarbonara. Optimization Strategies of Hysteretic Tuned Mass Dampers for Seismic Control. In *Nonlinear Dynamics and Control*. Springer, Cham, 2020. 99 – 106.

Boccamazzo, A., B. Carboni, G. Quaranta, and W. Lacarbonara. Seismic effectiveness of hysteretic tuned mass dampers for inelastic structures.. In *Engineering Structures*, 216, 110591.

Bouc, R. Forced vibrations of mechanical systems with hysteresis. In *Proceedings of the Fourth Conference on Nonlinear Oscillations*, Prague, 1967.

Carboni, B., W. Lacarbonara, and F. Auricchio. Hysteresis of multiconfiguration assemblies of nitinol and steel strands: experiments and phenomenological identification. *Journal of Engineering Mechanics*, 141.3: 04014135, 2015.

Carboni, B. and W. Lacarbonara. Nonlinear vibration absorber with pinched hysteresis: theory and experiments. *Journal of Engineering Mechanics*, 142.5: 04016023, 2016.

Carboni, B. and W. Lacarbonara. Nonlinear dynamic characterization of a new hysteretic device: experiments and computations.. *Nonlinear Dynamics*, 83.1-2: 23 – 39, 2016.

Elias, S. and V. Matsagar. Research developments in vibration control of structures using passive tuned mass dampers.. *Annual Reviews in Control*, 44: 129 – 156, 2017.

NTC2018. Aggiornamento delle Norme Tecniche per le Costruzioni, Decree of the Minister of the Infrastructures, 14, 2018.

Storn, R. and K. Price. Differential evolution–a simple and efficient heuristic for global optimization over continuous spaces. *Journal of global optimization*, 11.4: 341 – 359, 1997.

Wen, Y. K. Method for random vibration of hysteretic systems. *Journal of the engineering mechanics division*, 102.2: 249 – 263, 1976.

Wong, K. K. and J.L. Harris. Seismic damage and fragility analysis of structures with tuned mass dampers based on plastic energy.. *The Structural Design of Tall and Special Buildings*, 21.4: 296 – 310, 2012.